

REPORT DOCUMENTATION PAGE				Form Approved OMB NO. 0704-0188	
<p>The public reporting burden for this collection of information is estimated to average 1 hour per response, including the time for reviewing instructions, searching existing data sources, gathering and maintaining the data needed, and completing and reviewing the collection of information. Send comments regarding this burden estimate or any other aspect of this collection of information, including suggestions for reducing this burden, to Washington Headquarters Services, Directorate for Information Operations and Reports, 1215 Jefferson Davis Highway, Suite 1204, Arlington VA, 22202-4302. Respondents should be aware that notwithstanding any other provision of law, no person shall be subject to any penalty for failing to comply with a collection of information if it does not display a currently valid OMB control number.</p> <p>PLEASE DO NOT RETURN YOUR FORM TO THE ABOVE ADDRESS.</p>					
1. REPORT DATE (DD-MM-YYYY)		2. REPORT TYPE New Reprint		3. DATES COVERED (From - To) -	
4. TITLE AND SUBTITLE A Man-Portable Vector Sensor for Identification of Unexploded Ordnance				5a. CONTRACT NUMBER W911NF-08-1-0385	
				5b. GRANT NUMBER	
				5c. PROGRAM ELEMENT NUMBER	
6. AUTHORS Juan Pablo Fernandez, Benjamin E. Barrowes, Tomasz M. Grzegorzczuk, Nicolas Lhomme, Kevin O'Neill, Fridon Shubitidze				5d. PROJECT NUMBER	
				5e. TASK NUMBER	
				5f. WORK UNIT NUMBER	
7. PERFORMING ORGANIZATION NAMES AND ADDRESSES Dartmouth College Office of Sponsored Projects Trustees of Dartmouth College Hanover, NH 03753 -1404				8. PERFORMING ORGANIZATION REPORT NUMBER	
9. SPONSORING/MONITORING AGENCY NAME(S) AND ADDRESS(ES) U.S. Army Research Office P.O. Box 12211 Research Triangle Park, NC 27709-2211				10. SPONSOR/MONITOR'S ACRONYM(S) ARO	
				11. SPONSOR/MONITOR'S REPORT NUMBER(S) 55000-EV.4	
12. DISTRIBUTION AVAILABILITY STATEMENT Approved for public release; distribution is unlimited.					
13. SUPPLEMENTARY NOTES The views, opinions and/or findings contained in this report are those of the author(s) and should not be construed as an official Department of the Army position, policy or decision, unless so designated by other documentation.					
14. ABSTRACT The identification and discrimination of unexploded ordnance using low-frequency electromagnetic induction is an expensive and difficult process, typically beset by low data diversity and high positioning uncertainty. In this paper, we present the Man-Portable Vector (MPV) sensor, a new time-domain instrument					
15. SUBJECT TERMS Sensor, UXO					
16. SECURITY CLASSIFICATION OF:			17. LIMITATION OF ABSTRACT UU	15. NUMBER OF PAGES	19a. NAME OF RESPONSIBLE PERSON Fridon Shubitidze
a. REPORT UU	b. ABSTRACT UU	c. THIS PAGE UU			19b. TELEPHONE NUMBER 603-646-3671

## **Report Title**

A Man-Portable Vector Sensor for Identification of Unexploded Ordnance

### **ABSTRACT**

The identification and discrimination of unexploded ordnance using low-frequency electromagnetic induction is an expensive and difficult process, typically beset by low data diversity and high positioning uncertainty. In this paper, we present the Man-Portable Vector (MPV) sensor, a new time-domain instrument designed to remedy these shortcomings by measuring all three vector components of the secondary magnetic field at five distinct points around each transmitter location. The MPV also has a laser positioning system that can give its location with millimeter precision. After describing the instrument in detail, we study its performance in various sets of measurements, using the tensor dipole model to analyze the data. We find that the sensor can detect deeply buried targets and identify some standard ordnance items. It can also resolve separate targets in cases where two objects share the field of view and produce overlapping signals. A new incarnation of the MPV, the MPV-II, is in an advanced stage of development.

Index Terms—E



---

**REPORT DOCUMENTATION PAGE (SF298)**  
**(Continuation Sheet)**

---

Continuation for Block 13

ARO Report Number    55000.4-EV  
A Man-Portable Vector Sensor for Identification    ...

Block 13: Supplementary Note

© 2011 . Published in IEEE Sensors Journal, Vol. Ed. 0 11, (10) (2011), ( (10). DoD Components reserve a royalty-free, nonexclusive and irrevocable right to reproduce, publish, or otherwise use the work for Federal purposes, and to authroize others to do so (DODGARS §32.36). The views, opinions and/or findings contained in this report are those of the author(s) and should not be construed as an official Department of the Army position, policy or decision, unless so designated by other documentation.

Approved for public release; distribution is unlimited.

# A Man-Portable Vector Sensor for Identification of Unexploded Ordnance

Juan Pablo Fernández, Benjamin E. Barrowes, *Member, IEEE*, Tomasz M. Grzegorzczak, *Senior Member, IEEE*, Nicolas Lhomme, Kevin O'Neill, and Fridon Shubitidze, *Senior Member, IEEE*

**Abstract**—The identification and discrimination of unexploded ordnance using low-frequency electromagnetic induction is an expensive and difficult process, typically beset by low data diversity and high positioning uncertainty. In this paper, we present the Man-Portable Vector (MPV) sensor, a new time-domain instrument designed to remedy these shortcomings by measuring all three vector components of the secondary magnetic field at five distinct points around each transmitter location. The MPV also has a laser positioning system that can give its location with millimeter precision. After describing the instrument in detail, we study its performance in various sets of measurements, using the tensor dipole model to analyze the data. We find that the sensor can detect deeply buried targets and identify some standard ordnance items. It can also resolve separate targets in cases where two objects share the field of view and produce overlapping signals. A new incarnation of the MPV, the MPV-II, is in an advanced stage of development.

**Index Terms**—Electromagnetic induction (EMI), man-portable vector (MPV) sensor, unexploded ordnance (UXO).

## I. INTRODUCTION

THE PRESENCE of buried unexploded ordnance (UXO) in former battlefields and decommissioned firing ranges is an increasingly serious humanitarian and environmental problem worldwide [1], [2], with timescales measured in decades and yearly casualty rates in the hundreds. UXO cleanup is extremely expensive and laborious, reaching some \$1.4 million per acre in the United States [3], because most environments that contain UXO are also cluttered with harmless items that get detected just as readily and, in the absence of further information, must be treated as dangerous. Thus the

Manuscript received November 23, 2010; revised January 28, 2011; accepted February 15, 2011. Date of publication February 22, 2011; date of current version August 24, 2011. This work was supported in part by the U.S. Army Corps of Engineers, Engineer Research and Development Center UXO EQ/I program, in part by the Strategic Environmental Research and Development Program, Projects MM-1443, MM-1537, and MM-1637, and in part by the Environmental Security Technology Certification Program, Project MR-201005. The associate editor coordinating the review of this manuscript and approving it for publication was Dr. Patrick Ruther.

J. P. Fernández is at 88 Franklin St. Unit 301, Lynn, MA 01902-4171 USA (e-mail: jpf@alumni.umass.edu).

B. Barrowes and K. O'Neill are with the U.S. Army Corps of Engineers, ERDC-CRREL, Hanover, NH 03755 USA.

T. M. Grzegorzczak is with Delpsi, LLC, Newton, MA 02458 USA.

N. Lhomme is with Sky Research, Inc., Vancouver, BC V6T 1Z3, Canada.

F. Shubitidze is with the Thayer School of Engineering, Dartmouth College, Hanover, NH 03755 USA.

N. Lhomme is with Sky Research, Vancouver, BC V6T 1Z3, Canada.

Color versions of one or more of the figures in this paper are available online at <http://ieeexplore.ieee.org>.

Digital Object Identifier 10.1109/JSEN.2011.2118200



Fig. 1. MPV sensor with the ArcSecond positioning system. The sensor head is about 75 cm in diameter; see Fig. 2 for the other dimensions.

technical problem is not one of detection but one of identification and discrimination. Electromagnetic induction (EMI) sensing, in which a primary field established by a sensor induces eddy currents and magnetic response in metallic bodies [4] in a frequency range at which the ground is essentially transparent, is considered a most promising technique in the field; however, it is not exempt from difficulties.

Induction sensing occurs at very low electromagnetic frequencies, which means that one must work at very low resolutions and forfeit the possibility of imaging to search instead for patterns or signatures in the data. This shortage of information is exacerbated by the very small spatial diversity of the measurements, which often consist of a single field component measured at a single altitude at only a few points, and by the strong influence of sensor positioning and its uncertainty on the detected signal. New-generation instruments like the Berkeley UXO Discriminator (BUD) [5], [6], TEMTADS [7], and the MetalMapper [8], [9] attempt to ameliorate this situation by providing arrays of transmitters and receivers in precisely known configurations; these systems, however, are large and heavy and cannot be readily used in rough or treed terrain that does not allow vehicular access.

The Man-Portable Vector (MPV) sensor [10], shown in Fig. 1 and schematically in Fig. 2, has been designed in response to the previous concerns. Developed by G&G Sciences, the MPV is a mono/multistatic ultrawideband time-domain handheld EMI instrument that measures all three components of the secondary

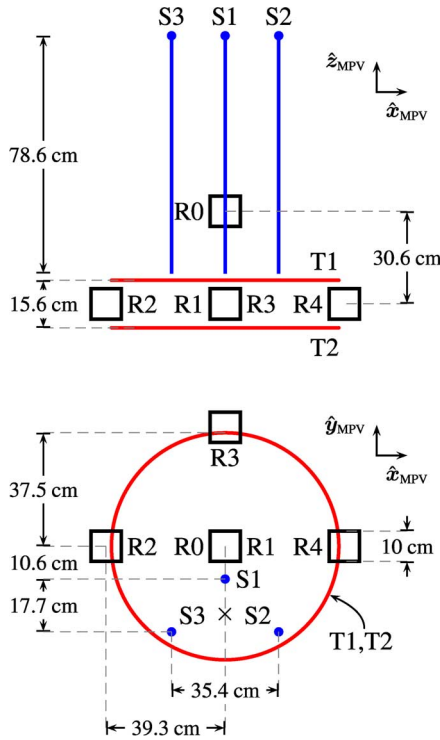


Fig. 2. Sketch of the MPV from behind (top panel) and from above (bottom panel). The red circles of radius 37.5 cm are the two transmitter coils, described more fully in Section II-A. Their finite heights have been neglected. The black squares of side 10 cm represent the receivers, with R1 at the center, R0 located 30.6 cm above it (in the  $+\hat{z}_{MPV}$  direction), and the others separated from R1 by 39.3 cm: R2 in the  $-\hat{x}_{MPV}$  direction, R3 in  $+\hat{y}_{MPV}$ , and R4 in  $+\hat{x}_{MPV}$ . These are described in detail in Section II.B. The ArcSecond receivers of Section II-C, arranged in an isosceles right triangle above and behind the receiver assembly, are represented by large blue dots.

field at five different locations—in particular at two different heights—with user-adjustable temporal resolution and data-acquisition window, either in static or dynamic measurement configurations. It is equipped with a laser positioning system that tracks its location with sub-centimeter precision. It also records the transmitter current at every point, which can be used to cancel errors in this current due to instrument drift. These features, along with its portability, make the MPV a highly versatile instrument that provides a wealth of high-quality information.

Several previous studies [11]–[13] have shown that the MPV is indeed a capable tool for detection and identification of buried items. MPV-collected data have been analyzed using the dipole model [14], the Standardized Excitation Approach [15] and a generalized version thereof [12], and the Normalized Surface Magnetic Source (NSMS) method [11], [16], [17] to detect and identify single- and multiple-target UXO scenarios in the laboratory and at various UXO sites. Future plans include the adaptation to the MPV of the Orthogonal Volume Magnetic Source model [18] and of spheroidal [19], [20] and ellipsoidal [21] analytic procedures.

In this paper, we aim to present the MPV in detail and use MPV data to perform some examples of identification tasks using the tensor dipole model, which has worked well with other instruments, both in the frequency domain [22]–[26] and in the time domain [27]. This method, which characterizes a target using a symmetric polarizability tensor [28], allows reasonable

estimation of the location and orientation of a buried object and yields an intrinsic electromagnetic signature that can be analyzed further—for example, by checking it against a standardized set previously stored in a library. The next step—use of this identifying information to classify buried targets and ultimately to discriminate UXO from clutter—is beyond the scope of this paper but has been performed successfully starting from MPV data [15], [16].

The paper is organized as follows. In Section II, we present the MPV sensor, describing its features and positioning system and addressing some of the special data-processing procedures required by them. In Section III, we introduce the dipole model and use it to give a few examples of one- and two-target identification and discrimination starting from MPV data. In Section IV, we present the MPV-II, a forthcoming streamlined and more ergonomic version of the MPV, and in Section V we conclude.

## II. MPV SENSOR

The MPV is a hybrid monostatic/multistatic sensor. The transmitters and receivers are rigidly attached and move in lockstep, but for each sensor location (transmitter sequence or “data shot”) there are five receiver locations and three vector components at each receiver, for a total of 15 usable measurements. Sensor positioning is currently tracked using an ArcSecond laser system (the gray PVC masts appearing in Fig. 1) that maintains accuracies on the order of a few millimeters. The sensor is designed to achieve a high SNR with a large dynamic range. It can in principle be used for ordinary surveying or for close interrogation of anomalies previously detected by other methods.

The MPV can be operated in two distinct data-acquisition modes: static and dynamic. In both modes, the MPV collects positioning and magnetic field data at a rate of 10 Hz. The 100-ms cycle is described further in Section II-A. In static data-acquisition mode the instrument is placed in a fixed location—typically at a set of approximate grid points over a specific anomaly—and the 10-Hz data are stacked, or averaged, for an amount of time that can be selected by the user. This mode results in a higher SNR compared to that of the dynamic data mode due to the noise-reducing effect of integration, but the resulting data are fairly sparse. Using the MPV in dynamic mode results in 10-Hz data collection points as the MPV is freely waved around above an anomaly. While the SNR is lower in this mode, the data are potentially more diverse because the instrument can be maneuvered to interrogate the anomaly from different angles and depths. The data are also more abundant: half a minute’s worth of target illumination results in  $300 \times 5 \times 3 = 4500$  data points, not including the number of time gates chosen for each. We shall concentrate on the static mode in this paper; we note, however, that it is equally possible to perform UXO discrimination starting from dynamic data [11], [29].

### A. Transmitter Coils

The transmitter assembly of the MPV consists of two circular parallel coils of radius 37.5 cm whose centers lie on a line perpendicular to the planes of the circles; the distance between the



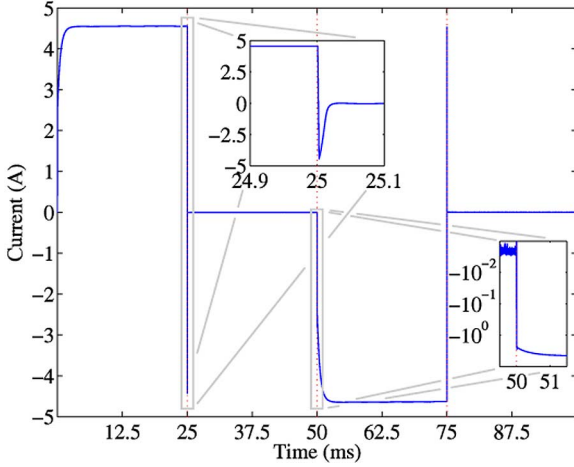


Fig. 3. MPV transmitter cycle. The plot shows a typical bipolar on/off cycle of the MPV transmitter assembly. The total duration is 100 ms, divided into four stages of equal duration (separated by vertical dotted lines): A step-on that plateaus at about 4.5 A, a step-off (shown in detail in the top left inset), a step-on of opposite polarity, and another step-off. The bottom right inset shows the second (“negative”) turn-on stage; we use a logarithmic  $y$ -axis to bring attention to a small peak that occurs between the first, more abrupt rise and the damped one that ends in a stable value. In actual measurements only the step-on currents are recorded. The data acquisition system has a sampling rate of  $2 \mu\text{s}$ ; the plot thus contains  $5 \times 10^4$  data points. Each point has resulted from stacking 100 measurements.

bottom of the upper transmitter and the top of the lower transmitter is 11.6 cm. The bottom of lower transmitter coil is 0.7 cm from the bottom surface of the plywood framework that houses it. Each coil is about 4.8 cm tall and is composed of 14 helically wound copper-wire loops, each of which has diameter 2 mm and is vertically separated from its neighbors by approximately 1.5 mm end to end. These coils vertically bracket most of the receiver assembly to be discussed in the next subsection.

The transmitter works in the bipolar on/off cycle shown in Fig. 3. (These settings are in fact adjustable; here we restrict our attention to the numbers used most often in the measurements reported below.) A gradual but fairly rapid buildup of current occurs at the beginning of each cycle; after a couple of milliseconds the current plateaus and stabilizes at about 4.5 A. At 25 ms it is shut off abruptly and kept at zero for 25 ms more. Midway through the cycle the current is built up again, with the polarity reversed in order to limit the magnetization of the target during data collection and suppress long-lived eddy currents, and then shut off again at 75 ms for another 25 ms that conclude the cycle. Sharp spikes follow the shutoffs and, to a lesser extent, the onsets of the buildup stages; these are highlighted in the figure insets.

To make the data files more compact, only the current through the transmitter coils is measured during transmitter-on time; when the transmitter is turned off, only the voltages across the 15 receiver coils are recorded. The MPV thus gives a picture of the transmitter current when it is on, at different times than the receiver signals but sampled identically. The reason for sampling the transmitter current is to measure it near the end of its cycle, when it reaches its peak, because that is the magnitude of the driving signal that energizes a target: the driving field at the target ( $d\mathbf{B}/dt$  from the transmitter current) is approximately an impulse with a magnitude proportional to the current in the transmitting loop just before it turns off. The data have to be

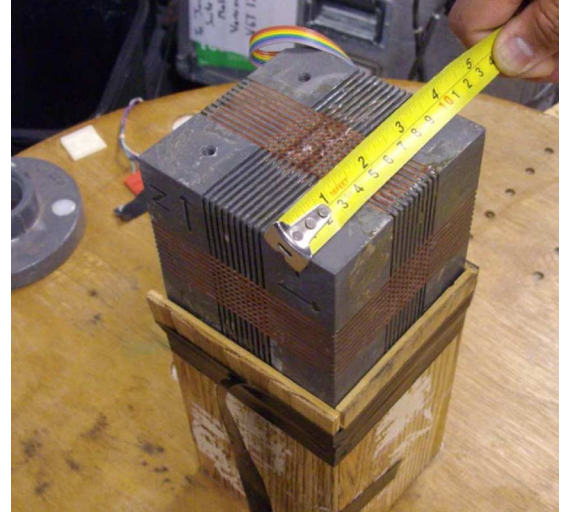


Fig. 4. Close-up view of one of the MPV cubes (R0 in this case) showing the three receiver coils. The numbers in the tape measure increase in the  $-\hat{x}_{\text{MPV}}$  direction.

normalized with respect to the transmitter current because the latter varies noticeably from point to point. Usually the measured voltage at each receiver coil is divided by the transmitted current read at the last time sample.

In the modeling examples that follow we neglect the heights of the coil assemblies and simulate the transmitters using an analytic expression for the primary field due to an infinitesimally thin circular loop of radius  $\chi$  placed flat on the  $x$ - $y$  plane and centered at the origin [30], [31]:

$$\mathbf{H}^{\text{Pr}}(\mathbf{r}) = \frac{I}{\pi} \nabla \times \frac{\hat{\phi}}{k} \sqrt{\frac{\chi}{\rho}} \left[ \left( 1 - \frac{1}{2} k^2 \right) K(k) - E(k) \right] \quad (1)$$

in cylindrical coordinates, where the modulus of the complete elliptic integrals  $K$  and  $E$  [32], [33] is

$$k^2 = \frac{4\rho\chi}{(\chi + \rho)^2 + z^2}. \quad (2)$$

We take the two thin loops to be separated by 15.6 cm.

### B. Receiver Cubes

The MPV receiver assembly consists of five triaxial coils wound around plastic cubes, numbered R0 through R4. Fig. 2 shows a diagram of the sensor as seen from above and from behind. In what follows we refer to the coordinate system shown in the figure as the “MPV”: the origin is at the center of receiver R1; the  $x$ -axis points from the origin to the center of receiver R4, the  $y$ -axis points to the center of receiver R3, and the  $z$ -axis points to the center of receiver R0. In that system, cube R0 is located above center ( $z = 30.6$  cm), cube R2 is left of center ( $x = -39.3$  cm), cube R3 is forward of center ( $y = 39.3$  cm), and cube R4 is right of center ( $x = 39.3$  cm).

Fig. 4 shows a close-up view of one of the cubes. Each air-cored receiver coil is wound helically on a set of ten grooves etched on the surface of the cube; 36-gauge wire is used throughout. Each groove is 1.2 mm wide and is separated from its neighbors by 2.0 mm; thus, each set of grooves has a total width of  $0.12 \times 10 + 0.2 \times 9 = 3.0$  cm. From Faraday’s

law, the measured signal must be interpreted as the surface integral of the time derivative of the secondary magnetic flux density; the dimensions of the MPV receiver coils have been chosen so the signals are as similar loop-to-loop as possible. The grooves corresponding to the  $z$ -coil (the horizontal one in Fig. 4) are 1.0 mm deep; each groove has 12 turns wound around it, giving the coil an effective flux-measuring area of  $120 \times (10.0 - 0.1 \times 2)^2 = 11524.8 \text{ cm}^2$ . The  $x$ -coil, perpendicular to the tape measure in Fig. 4, is wound around 4.8-mm deep horizontal grooves and 1.0-mm deep vertical ones and contains 13 turns per groove; its effective area is  $130 \times (10.0 - 2 \times 0.48) \times (10.0 - 2 \times 0.1) = 11517.0 \text{ cm}^2$ . Finally, the  $y$ -coil surrounds 4.66-mm deep grooves, and has 14 turns per groove, which gives it an effective area of  $140 \times (10.0 - 2 \times 0.466)^2 = 11512.0 \text{ cm}^2$ . In the inversions of Section III we take all receivers to be  $10 \times 10 \text{ cm}^2$ ; we also implicitly divide out the number of loops and neglect the groove-to-groove separation. These effects are not too dramatic unless the target is very close to the sensor, as has also been found to happen with other EMI instruments [34].

The MPV records a user-selectable number of time gates ranging from about 60  $\mu\text{s}$  to typically 25 ms. Common settings include 30 or 35 logarithmically spaced gates, but the MPV can also sample more than 100 time channels (as in Section III-B1). The signals from the cubes are amplified and sampled in a data-acquisition system tethered to the sensor (the backpack in Fig. 1).

### C. ArcSecond Positioning

Access to the full 3D response of a target makes it necessary to have a full 3D positioning system that accounts for the location and tilt angles of the sensor at any point. Some existing EMI sensors have used GPS for this purpose [5], [6], [35] though the available resolution, on the order of centimeters, serves to record anomaly locations for further study but sometimes does not suffice to support discrimination.

The MPV is equipped with an ArcSecond positioning system that consists of three receivers, S1, S2, and S3, whose locations are known with respect to a coordinate system (the “ASI”) provided by the positioning device. The ArcSecond receivers are arranged in an isosceles right triangle of side 25 cm placed so that the line pointing from the centroid of the triangle to the right angle coincides with  $\hat{\mathbf{y}}_{\text{MPV}}$  and the hypotenuse coincides with  $\hat{\mathbf{x}}_{\text{MPV}}$ . The centroid of the triangle is located 22.4 cm behind receiver R0 (see Fig. 2.) In terms of the ASI receiver locations we have the MPV unit vectors [36]

$$\hat{\mathbf{x}}_{\text{MPV}} = \frac{\mathbf{r}_{\text{S2}} - \mathbf{r}_{\text{S3}}}{|\mathbf{r}_{\text{S2}} - \mathbf{r}_{\text{S3}}|} \quad (3a)$$

$$\hat{\mathbf{y}}_{\text{MPV}} = \frac{\mathbf{r}_{\text{S1}} - \frac{1}{2}(\mathbf{r}_{\text{S2}} + \mathbf{r}_{\text{S3}})}{|\mathbf{r}_{\text{S1}} - \frac{1}{2}(\mathbf{r}_{\text{S2}} + \mathbf{r}_{\text{S3}})|} \quad (3b)$$

$$\hat{\mathbf{z}}_{\text{MPV}} = \hat{\mathbf{x}}_{\text{MPV}} \times \hat{\mathbf{y}}_{\text{MPV}} \quad (3c)$$

which in turn yield the rotation matrix (also called “direction cosine matrix, or DCM”)

$$\mathbf{R} = \begin{bmatrix} \hat{\mathbf{x}}_{\text{MPV}} \cdot \hat{\mathbf{x}} & \hat{\mathbf{x}}_{\text{MPV}} \cdot \hat{\mathbf{y}} & \hat{\mathbf{x}}_{\text{MPV}} \cdot \hat{\mathbf{z}} \\ \hat{\mathbf{y}}_{\text{MPV}} \cdot \hat{\mathbf{x}} & \hat{\mathbf{y}}_{\text{MPV}} \cdot \hat{\mathbf{y}} & \hat{\mathbf{y}}_{\text{MPV}} \cdot \hat{\mathbf{z}} \\ \hat{\mathbf{z}}_{\text{MPV}} \cdot \hat{\mathbf{x}} & \hat{\mathbf{z}}_{\text{MPV}} \cdot \hat{\mathbf{y}} & \hat{\mathbf{z}}_{\text{MPV}} \cdot \hat{\mathbf{z}} \end{bmatrix}. \quad (4)$$

At each step the DCM can be polished (i.e., made “more orthogonal”) by iterating [37]

$$\mathbf{R}_{n+1} = \frac{1}{2} \left( \mathbf{R}_n + (\mathbf{R}_n^T)^{-1} \right) \quad (5)$$

starting from the initially measured  $\mathbf{R}_0$ . Usually three iterations are sufficient. From the DCM we can compute the Euler angles in the yaw-pitch-roll convention [38], modified so that  $\hat{\mathbf{x}} \rightarrow \hat{\mathbf{y}}$ ,  $\hat{\mathbf{y}} \rightarrow \hat{\mathbf{x}}$ ,  $\hat{\mathbf{z}} \rightarrow -\hat{\mathbf{z}}$  [36]:

$$\phi = \arctan \frac{\hat{\mathbf{y}}_{\text{MPV}} \cdot \hat{\mathbf{x}}}{\hat{\mathbf{y}}_{\text{MPV}} \cdot \hat{\mathbf{y}}} \quad \text{Yaw} \quad (6a)$$

$$\theta = \arcsin \frac{\hat{\mathbf{y}}_{\text{MPV}} \cdot \hat{\mathbf{z}}}{\hat{\mathbf{y}}_{\text{MPV}} \cdot \hat{\mathbf{z}}} \quad \text{Pitch} \quad (6b)$$

$$-\psi = \arctan \frac{\hat{\mathbf{x}}_{\text{MPV}} \cdot \hat{\mathbf{z}}}{\hat{\mathbf{z}}_{\text{MPV}} \cdot \hat{\mathbf{z}}} \quad \text{Roll.} \quad (6c)$$

A relevant measurable parameter is the “tilt angle” of the MPV, defined by

$$\gamma = \arccos(\hat{\mathbf{z}}_{\text{MPV}} \cdot \hat{\mathbf{z}}) \quad (7)$$

which in terms of the Euler angles is

$$\cos \gamma = \cos \psi \cos \theta. \quad (8)$$

This expression is independent of yaw and has a different interpretation for cases with pure pitch than in cases with pure roll, allowing us to check the correctness of each angle separately.

Next we locate the MPV and its receivers. The ASI triangle is centered at the point

$$\mathbf{R}_c = \frac{1}{3}(\mathbf{r}_{\text{S1}} + \mathbf{r}_{\text{S2}} + \mathbf{r}_{\text{S3}}) \quad (9)$$

and from the information in Fig. 2 we can locate every other point on the sensor. For example, the “center” of the MPV (i.e., the position of receiver R1) is

$$\mathbf{r}_{\text{R1}} = \mathbf{R}_c + 22.4 \hat{\mathbf{y}}_{\text{MPV}} - ((81.5 - 5.9/2) + 21.8/2) \hat{\mathbf{z}}_{\text{MPV}} \text{ cm.} \quad (10)$$

Fig. 5 shows an example measurement. With the MPV initially flat, the experimenter lifted the right-hand side ( $\hat{\mathbf{x}}_{\text{MPV}}$ ) of the sensor to an angle of about 20 degrees and then, always with a point on the bottom rim of the instrument in contact with a flat surface, and the opposite side in the air at about the same initial angle, in one smooth motion performed the cycle

$$\begin{aligned} \hat{\mathbf{x}}_{\text{MPV}} \text{ up} &\longrightarrow \hat{\mathbf{y}}_{\text{MPV}} \text{ up} \longrightarrow -\hat{\mathbf{x}}_{\text{MPV}} \text{ up} \\ &\longrightarrow -\hat{\mathbf{y}}_{\text{MPV}} \text{ up} \longrightarrow \hat{\mathbf{x}}_{\text{MPV}} \text{ up} \end{aligned}$$

and at the end laid the MPV flat again, pointing in the initial direction. (This motion somewhat resembles that of a slowly spinning coin.) Fig. 5(a) shows the location of the ASI triangle as the sensor moved, taken directly from the MPV readings. The protruding lines (not to scale) represent the unit vector  $\hat{\mathbf{z}}_{\text{MPV}}$ , which, as expected, is tilted at a constant angle and is seen to trace a circle. The dots at the bottom show the receiver R1, which barely moves during the process. Fig. 5(b) depicts the



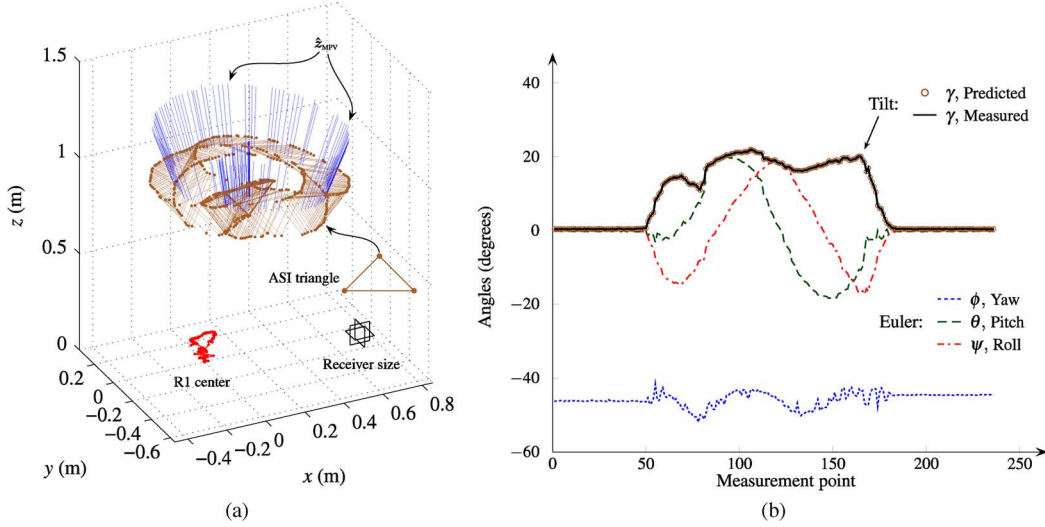


Fig. 5. Test of the ASI positioning system on the MPV. An experiment was carried out in which the MPV was tilted and cycled in a smooth motion reminiscent of that of a tilted spinning coin. (a) Location of the ASI triangle (brown) as the sensor moves, the footprint of the (barely moving) bottom central receiver R1 (red), and the tilted  $\hat{z}_{MPV}$ -axis (blue lines, with arrows removed to decrease clutter). The sizes of the triangle and a receiver are shown for reference. (b) Euler angles (dashed lines) in the yaw-pitch-roll convention, showing good agreement between the two expressions (7) (solid line) and (10) (circles) for the tilt angle  $\gamma$ .

Euler angles as computed from (6); the agreement between expressions (7) and (8) for the tilt angle  $\gamma$  shows that the pitch, yaw, and roll are determined correctly.

### III. EXAMPLE INVERSIONS USING THE MPV

#### A. Dipole Model

A popular and useful technique for UXO discrimination with EMI sensors models a buried target by a point dipole. The model has been implemented in the frequency domain [24], [22] and in the time domain [27] and has been found to fit measured data adequately when the targets are small enough—or far enough away from the sensor—that the primary field can be assumed uniform along their extent, and when their composition is homogeneous enough that there are no conflicting signals from different parts of the object [23], [39].

The dipole model postulates that for a given object it is possible to find a set of orthonormal axes ( $\hat{a}, \hat{b}, \hat{c}$ ) such that an external monochromatic magnetic field pointing along one of those directions induces a steady-state dipole moment parallel to it:

$$m_a = \beta_a H_a^{\text{pr}}, \quad m_b = \beta_b H_b^{\text{pr}}, \quad m_c = \beta_c H_c^{\text{pr}}. \quad (11)$$

For a primary field pointing in an arbitrary direction in the laboratory system, (11) becomes [23]

$$\mathbf{m} = \mathbf{R}_{abc} \mathbf{\Lambda} \mathbf{R}_{abc}^T \mathbf{H}^{\text{pr}} \equiv \mathbf{B} \mathbf{H}^{\text{pr}} \quad (12)$$

where  $\mathbf{R}_{abc}$  is an orthogonal DCM like (4) and  $\mathbf{\Lambda}$  is a diagonal matrix whose elements are the  $\beta_i$  from (11). The “polarizability tensor”  $\mathbf{B}$  is a symmetric  $3 \times 3$  matrix with dimensions of volume [28]. The secondary field is given by the standard dipole expression [40], [41]

$$\mathbf{H}^{\text{sc}}(\mathbf{r}) = \frac{1}{4\pi R^5} (3\mathbf{R}(\mathbf{R} \cdot \mathbf{m}) - R^2 \mathbf{m}) \quad (13)$$

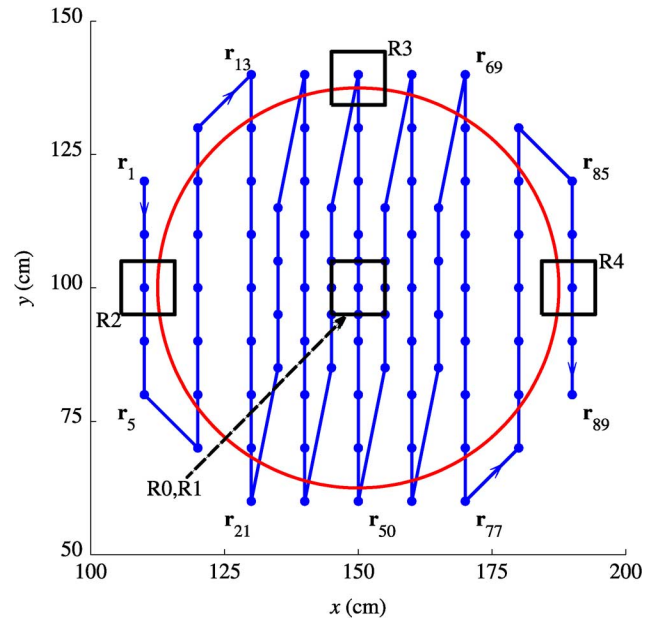


Fig. 6. Grid used for MPV test-stand measurements. The data runs start at point  $\mathbf{r}_1$  on the upper left corner and follow the blue line until point  $\mathbf{r}_{89} = 190\hat{x} + 80\hat{y}$  cm on the lower right corner; each is preceded and followed by calibration measurements, some 180 cm away from the center. Superimposed is a schematic diagram of the sensor, shown in more detail in Fig. 2.

where  $\mathbf{R} = \mathbf{r} - \mathbf{r}'$ ,  $\mathbf{r}$  is the observation point, and  $\mathbf{r}'$  is the location of the point dipole. In observance of Faraday’s law, EMI receivers measure not the field (13) but rather (the negative of) the time derivative of the flux through them. The time-domain signal measured at the  $k$ th time gate by receiver  $R_\mu$  ( $\mu = 0, \dots, 4$ ) along the  $\nu$ th ( $\nu = z, y, x$ ) direction when the sensor is centered at  $\mathbf{r}_j$  is thus

$$S_{\mu\nu}(\mathbf{r}_j, t_k) = \int_{R_\mu(\mathbf{r}_j)} ds_{R_\mu} \hat{n}_\nu \cdot \left[ \frac{1}{4\pi R^5} (3\mathbf{R}(\mathbf{R} \cdot \mathbf{p}(\mathbf{r}_j, t_k)) - R^2 \mathbf{p}(\mathbf{r}_j, t_k)) \right] \quad (14)$$

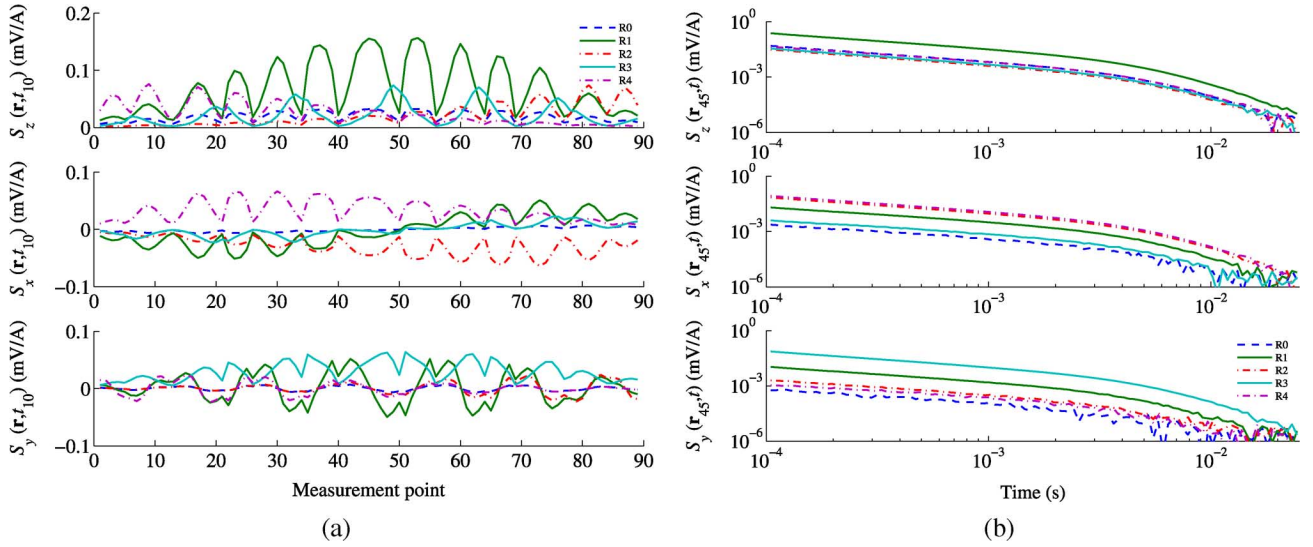


Fig. 7. Raw data taken by the MPV in Vicksburg. This particular data set has an upright 81-mm projectile as target, located 45 cm below the sensor. (a) Point-to-point values at the 10th time gate (0.168 ms after shutoff in this case) in the (from top to bottom)  $z$ ,  $x$ , and  $y$  directions. (b) Time development (in absolute value) at point  $\mathbf{r}_{45}$ , right at the center of the grid. The data has been normalized by the current at every point, and a background field taken some 180 cm away with no targets present (and smaller by four orders of magnitude) has been subtracted. The signals are clearly discernible until they decay below  $10^{-5}$  mV/A, at which point they are overwhelmed by noise.

where

$$\mathbf{p}(\mathbf{r}_j, t_k) = -\mu_0 \frac{d}{dt} [\mathbf{B}(t) * \mathbf{H}^{\text{pr}}(\mathbf{r}' - \mathbf{r}_j, t)] \Big|_{t=t_k} \quad (15)$$

the asterisk denotes a convolution [4], [42], and the primary field is that of (1) adapted to two vertically separated coils. An approximate simplified expression is obtained if the time development of the primary field is modeled by a Heaviside step-off at  $t = 0$  [43, p. 118]:

$$\begin{aligned} \mathbf{p}(\mathbf{r}_j, t_k) &= [\mu_0 \mathbf{B}(t = t_k) I_0] \mathbf{H}^{\text{pr}}(\mathbf{r}' - \mathbf{r}_j, t = 0) / I_0 \\ &\equiv \mathbf{R}_{abc} \Lambda(t_k) \mathbf{R}_{abc}^T \mathbf{H}^{\text{pr}}(\mathbf{r}' - \mathbf{r}_j) / I_0. \end{aligned} \quad (16)$$

Our definition of the time-domain response  $\Lambda(t_k)$  thus absorbs the medium permeability and  $I_0$ , the point-to-point final value of the current that produces the primary field, as discussed in Section II-A. A look at Fig. 3 shows that a step-off response like (16) represents a rather drastic simplification of what happens in reality. Moreover, we make no attempt to model  $\Lambda(t_k)$  or express it in terms of more fundamental quantities. This is a difficult problem [44] that has been solved analytically only for the sphere [40], [41], [45]–[47]. We content ourselves with extracting those principal elements and comparing them to “standard” versions stored in a library or verifying their case-to-case consistency. The Appendix describes a fast and accurate numerical implementation of the model which we use in subsequent sections.

### B. Data Acquisition

The MPV has been used to take data at several locations and in different experimental conditions.

1) *Vicksburg*: Researchers from G&G Sciences carried out in February and March of 2007 a series of test measurements [10] at the Waterways Experiment Station (WES), a facility of the U.S. Army Engineer Research and Development Center located in Vicksburg, MS. They took measurements on five targets—a

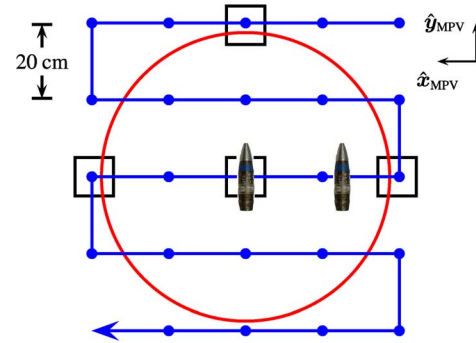


Fig. 8. Measurement grid for the measurement carried out at Sky Hanover. Note that the coordinate axes are flipped; as explained in the text, in this set of measurements the MPV was placed upside-down and the targets were moved around on a measurement grid above. The figure shows one typical setup, with two 40-mm projectiles separated horizontally by 25 cm.

BLU-26 bomblet and 57-mm, 60-mm, 81-mm, and 105-mm munitions—at different combinations of depth and orientation using the 89-point grid sketched in Fig. 6. The test stand at WES has a machined fiberglass platform over which a sensor, mounted on a robotic arm with computer-controlled motion, can be positioned to an accuracy of 1 mm; the targets are placed by remote controls, their depth known to within 1 cm. The background was measured at one faraway point before and after each data run. The sensor was firmly attached to the robotic arm so that its orientation was nominally constant throughout. Fig. 7 shows an example of the raw (though background-subtracted) data collected in Vicksburg. In the inversions of the next section we discard the first 15 time channels of the 122 that were used in this set of measurements. The measurements were repeated 27 times per data point and thus lasted for 2.7 s.

2) *Sky Hanover*: Personnel from Sky Research, Inc. carried out a series of measurements at their Hanover, New Hampshire, branch in March of 2009. This set of measurements differs from the others in that the sensor was placed *upside-down* on an adjustable support assembly and left in place throughout the data

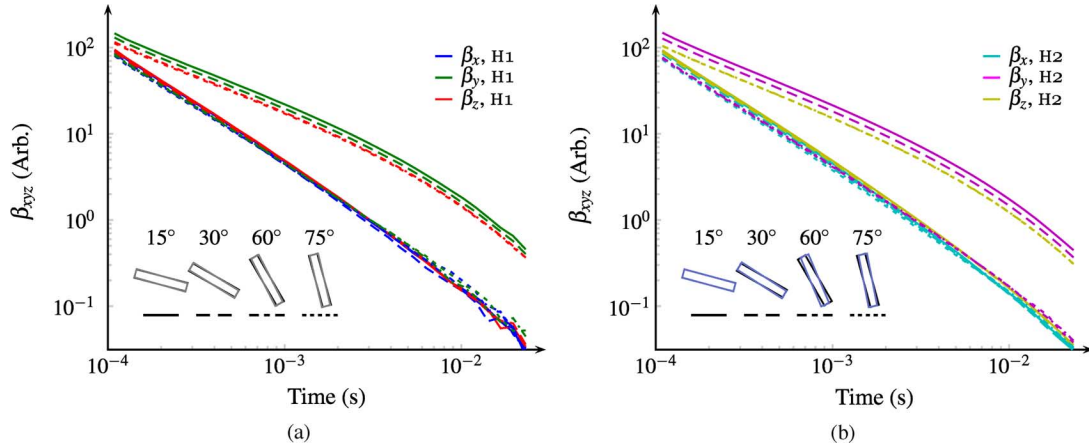


Fig. 9. One of the measurements performed in Vancouver on a cylinder of length 12'' and diameter 3''. The MPV collected data on a  $7 \times 7$  grid; the cylinder lay on a pivot of controllable angle. The experiment was performed at two different target depths—(a) and (b), respectively. The polarizability elements are consistent case to case. The tilt angles (measured values in black; model predictions in shades of gray) are also very close. Table I shows the results of the inversion.

TABLE I  
INVERTED AND MEASURED DEPTHS AND DIRECTIONS OF A 12-IN CYLINDER (A SMALL COMPONENT ALONG  $\hat{x}$  IS NOT SHOWN)

Dip ( $^\circ$ )	$\hat{\rho}_{\text{meas}}$	$\hat{\rho}_{\text{invr}}$	$h_{\text{meas}}$ (cm)	$h_{\text{invr}}$ (cm)	Discr. (%)
15	$+0.96\hat{y} - 0.26\hat{z}$	$+0.96\hat{y} - 0.27\hat{z}$	41.18	44.24	7.43
30	$+0.87\hat{y} - 0.50\hat{z}$	$+0.85\hat{y} - 0.52\hat{z}$	41.80	43.26	3.49
45	$-0.71\hat{y} + 0.71\hat{z}$	$+0.77\hat{y} - 0.64\hat{z}$	50.69	51.75	2.09
60	$-0.50\hat{y} + 0.87\hat{z}$	$-0.45\hat{y} + 0.89\hat{z}$	43.90	42.66	2.82
75	$-0.26\hat{y} + 0.97\hat{z}$	$-0.23\hat{y} + 0.97\hat{z}$	44.99	42.96	4.51
15	$+0.96\hat{y} - 0.26\hat{z}$	$+0.96\hat{y} - 0.26\hat{z}$	25.18	28.01	11.24
30	$+0.87\hat{y} - 0.50\hat{z}$	$+0.84\hat{y} - 0.54\hat{z}$	25.80	26.78	3.80
45	$-0.71\hat{y} + 0.71\hat{z}$	$-0.67\hat{y} + 0.74\hat{z}$	27.19	25.50	6.22
60	$-0.50\hat{y} + 0.87\hat{z}$	$-0.39\hat{y} + 0.92\hat{z}$	27.40	25.33	7.55
75	$-0.25\hat{y} + 0.97\hat{z}$	$-0.19\hat{y} + 0.98\hat{z}$	28.99	25.72	11.28

collection process while the targets were moved around, again in a snakelike fashion, on a  $5 \times 5$  measurement grid with 20 cm point-to-point separation (see Fig. 8) that rested on a door atop a stack of milk crates.

All measurements involved two-target configurations and employed 30 time channels (for inversion purposes we start with the second). Two stacks, each with 27 repetitions, were used, for a measurement duration of 5.4 s per data point. Some of the targets—the 60-mm, 81-mm, and 105-mm shells from the preceding section—had already been characterized at Vicksburg. A 40-mm projectile was also studied in this run, as were a ferrous ellipsoid and a box of nails to represent clutter.

3) *Sky Vancouver*: Another set of measurements taken by Sky Research staff took place in their Vancouver, British Columbia, office in February and March of 2010. The objects studied in this data run were not actual munitions but a diverse sampling of cylinders of sizes and material properties typical of UXO. Several one- and two-target scenarios were studied, along with attitude configurations similar to the one of Fig. 5 and time-on measurements to get a complete picture of the waveform (as presented in Fig. 3). An assortment of grids were used during the measurements, the most common being a  $7 \times 7$  grid with 15-cm separation, though for the multi-object measurements the favored grid was  $7 \times 6$ ; unlike the previous measurements, in this run the grids were navigated in zigzag, with the instrument moving in the same direction across every transect. A typical measurement included 27 repetitions (for a measurement time of 2.7 s per data point) and contained 35 time channels; in our inversions we discard the first of these.

### C. Results, One Target

We first look at some one-target inversions performed on the Vancouver MPV data. In one example, a solid steel cylinder of length 12'' (30.48 cm) and diameter 3 in (7.62 cm) was placed on a pivot with controllable dip angle. (See the inset of Fig. 9 for an example run.) Data were collected on the  $7 \times 7$  grid described previously with the cylinder pointing 15°, 30°, 60°, and 75° degrees below the horizontal; the experiment was performed at two different target depths. Fig. 9 and Table I display the results of the inversion for each case, including the reconstructed depth and the unit vector associated with the dominant eigenvalue; the  $\hat{x}$  component is always an order of magnitude smaller and is not displayed. (The table also displays the results of two additional measurements carried out at a 45° dip angle.) In all cases the agreement between measured and inverted locations and orientations is reasonable (as we can see from the last column, which displays the percent discrepancies in depth defined by  $|h_{\text{meas}} - h_{\text{invr}}|/h_{\text{meas}} \times 100$ ). The polarizability elements are consistent case to case and show the usual power-law/exponential decay [27], [48]; two of the elements, the “transverse” ones, are very similar to each other and thus reflect the azimuthal symmetry of the object. Note that there is an ambiguity in the orientation resulting from the cylinder’s up-down symmetry.

We can use the MPV data and our dipole inversion to investigate how the material properties of an object affect its EMI response. Fig. 10 shows the responses of two cylinders of identical size—length 6 in and diameter 3 in—placed at similar “depths.” (Two different experiments, at different depths and dip angles, are shown.) One of the cylinders is made of steel and the other



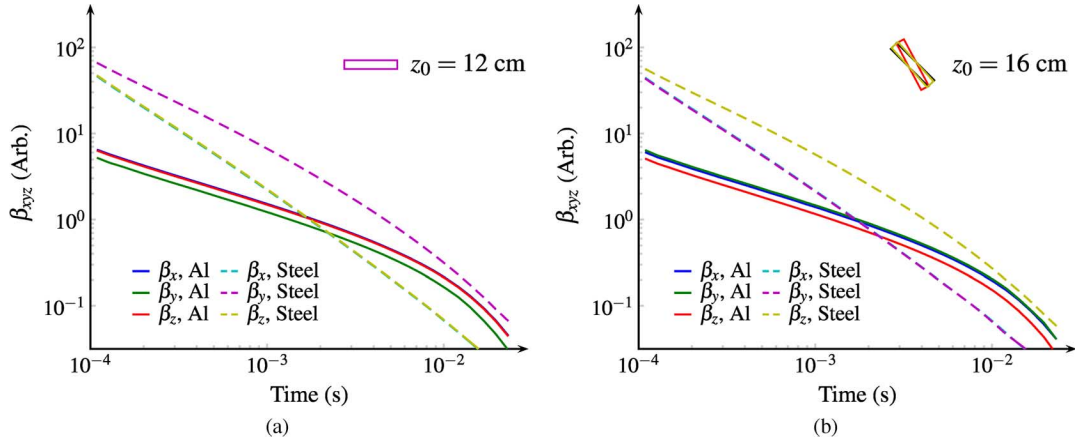


Fig. 10. Vancouver measurements on (aluminum and steel) cylinders of length 6 in and diameter 3 in. The MPV collected data on a  $7 \times 7$  grid. Two different target depths—(a) and (b), respectively—are shown for each cylinder. The polarizability elements of the nonferrous cylinder are “inverted” (in the sense that the longitudinal element is smaller than the transverse ones). They are also an order of magnitude smaller due to the higher conductivity of aluminum.

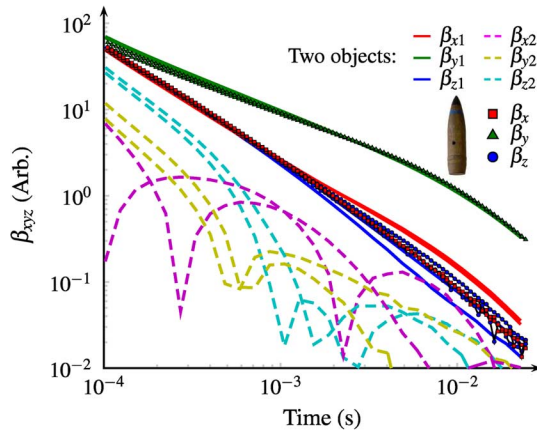


Fig. 11. Inverted time-dependent magnetic polarizabilities extracted from a multi-object MPV measurement. A 105-mm UXO and a box of nails are interrogated by the sensor on the  $5 \times 5$  grid of Fig. 8. Two separate experiments, involving different box/UXO separations (25 and 40 cm), are displayed. The larger response is consistent with that of the UXO in question; to confirm this we also plot the polarizabilities inverted from two independent one-target measurements carried out three years before.

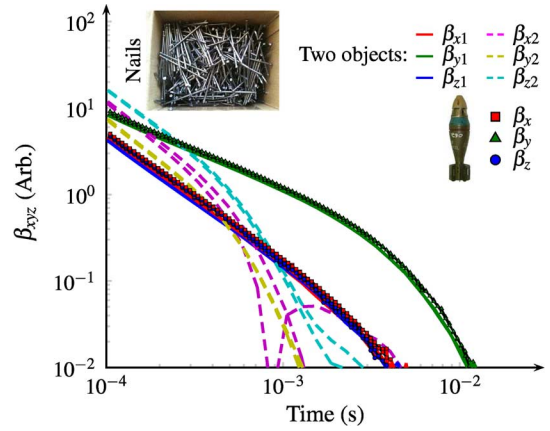


Fig. 12. Inverted time-dependent magnetic polarizabilities extracted from a multi-object MPV measurement. The setup is identical to that of Fig. 11, except that the UXO in this figure is a 60-mm mortar. The independent one-target data once again show good agreement for the UXO, while the box of nails—shown in the inset above—has a response similar to that on the other figure. Its quick decay despite its significant early-time value can be explained by EMI phenomenology.

is made of aluminum. Two features of the polarizability elements of nonferrous bodies stand out: 1) The longitudinal polarizability element is smaller than the two transverse ones for a non-ferrous body, the opposite of what happens with a ferrous object [49]; and 2) The polarizability elements of the aluminum cylinder are smaller than those of the steel cylinder by about an order of magnitude. The latter can be explained by the fact that the amplitude of the time derivative of the magnetic flux through the receivers—the quantity measured by the MPV—depends on the material properties of the target in the combination [45]  $\sim a/\sigma$ , where  $a$  is a characteristic length and  $\sigma$  is the conductivity. The conductivity of aluminum is  $\sigma_{\text{Al}} = 36.9$  MS/m, some six times that of steel,  $\sigma_{\text{Steel}} = 5.9$  MS/m [50]. On the other hand, the higher conductivity allows the induced eddy currents to linger on for a bit longer before their eventual exponential decay; this is also clearly visible from the figure.

#### D. Results, Two Targets

Figs. 11 and 12 show the inverted polarizabilities from some of the measurements taken at Sky Hanover and described in Section III-B2. In both cases a UXO is placed in the field of

view of the MPV alongside a full 5-lb box of nails used as a stand-in for clutter. In Fig. 11 the UXO is a 105-mm howitzer shell and in Fig. 12 it is a 60-mm mortar round; in all cases the munitions are horizontal. Each figure shows two different scenarios, with the box of nails placed 25 and 40 cm away (in the  $x$ -direction) from the ordnance and at the same depth. The figures show the inverted time-dependent polarizabilities.

In all cases the “first” object (solid lines) is readily identified as the corresponding UXO from its decay profile. The largest (“longitudinal”) polarizability element of the UXO is  $\beta_y$  in every case, consistent with the fact that the munition is horizontal and pointing in the  $\hat{y}_{\text{MPV}}$ -direction. (The corresponding eigenvector is almost exactly  $\hat{y}_{\text{MPV}}$  in all cases.) The transverse polarizability elements of the first object are again very similar, as expected from a body with azimuthal symmetry. To support the foregoing statements we have included in the figures (as dots) the inverted polarizabilities of the 105-mm and 60-mm UXO in two independent single-object characterization measurements taken over the 89-point grid at Vicksburg (Section III-B1). The inverted locations are displayed and compared to the ground truth in Table II. (The systematic error

TABLE II  
INVERTED TARGET LOCATIONS AND GROUND TRUTH FOR SELECTED  
VICKSBURG MEASUREMENTS

UXO	Model (cm)			Ground truth (cm)		
	$x$	$y$	$z$	$x$	$y$	$z$
105-mm	3.94	3.87	61.71	0	0	60
105-mm	3.79	3.40	42.52	0	0	40
60-mm	3.85	-1.35	46.71	0	0	45
60-mm	3.52	-1.78	26.85	0	0	25

of almost 4 cm in the  $x$ -coordinate had already been noted by the researchers that took the data [10].)

The “second” object (shown with dashed lines) produces a signal whose three elements are clearly different. This is to be expected, since the box has much less symmetry than the munitions. The polarizability elements from the second object decay much faster than those of the first, even though at early times they are of comparable magnitude (and can even be larger, as in Fig. 12). This behavior can be explained using EMI phenomenology [48], [51]: the metal in the box is packed in a loose and highly irregular manner, occupying a fairly large but not compact volume. (Its dimensions are  $\approx 11 \times 11 \times 14 \text{ cm}^3$  and its weight is 5 lb or 2.3 kg, which makes it intermediate between the two projectiles. To give a sense of the packing fraction we note that a steel cube of those dimensions would weigh some 30 lb.) At early times, when the eddy currents induced by the sensor are superficial, the response is sizable; later on, as the currents diffuse, they are hampered by the relatively large hollow spaces between the nails and dwindle quickly.

We note that the results are not as consistent measurement-to-measurement for the box as they are for the projectile. (Note in particular the appearance of sign flips.) The fact that the box has sharp corners makes it difficult to model it using a dipole. Also, in this experiment the sensor remained stationary while the targets were moved: the separation between the objects changes from point to point, however minutely, and the uncertainties accumulate; moreover, the nails within the box also move, however imperceptibly, from point to point, which also augments the inversion error. When the objects are placed at different depths, the results deteriorate somewhat for the box but are consistent for the UXO.

For a final example we return to the Vancouver measurements. Fig. 13 shows the polarizability elements extracted from two different two-target experiments. The dashed lines represent “Case 45,” where two copies of the 6-in cylinder studied in Fig. 10 were placed 50 cm apart at a depth of 52.5 cm. The solid lines correspond to “Case 67,” where one of the 6-in cylinders shared the field of view of the MPV with a smaller and thinner cylinder (length 4 in and diameter 1.5 in). For comparison we have included the polarizability elements of each of the cylinders as inverted from single-target data collected for those objects. The measurements are again quite consistent. Table III compares the inverted object locations to the measured ground truth. We remark that there seems to be a small systematic error in that the predicted depth is always slightly larger than the measurements. Moreover, some other cases from the Vancouver run do not lend themselves to easy inversion, especially for scenarios in which one object is very close to another and at a different height, with the extreme

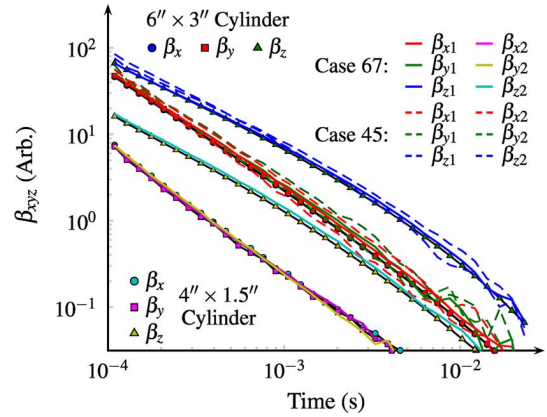


Fig. 13. Magnetic polarizabilities inverted from Vancouver one-target and two-target measurements. Case 45 (dashed lines) involves two copies of the 6 in  $\times$  3 in cylinder from Fig. 10 and Case 67 (solid lines) includes one of those cylinders and a smaller one of size 4 in  $\times$  3 in. For comparison, we have added the polarizabilities extracted from single-target data collected for those objects. The location predictions appear in Table III.

TABLE III  
INVERTED LOCATIONS AND GROUND TRUTH FOR SELECTED VANCOUVER  
TWO-TARGET MEASUREMENTS

ID	Model (cm)				Ground truth (cm)			
	$z_1$	$z_2$	$dz$	$dy$	$z_1$	$z_2$	$dz$	$dy$
45	56.5	57.9	1.4	50.0	52.5	52.5	0.0	50.0
67	41.8	34.2	7.6	50.0	38.5	31.0	7.5	50.0

situation of one target lying right above the other being, as expected, the hardest to treat [14].

We have seen in this section that the MPV provides data of sufficient quality that it allows the consistent identification of deeply buried targets. Using the MPV one can also discern composite signals due to two visually obscured objects in proximity to one another.

#### IV. MPV-II

Some shortcomings of the original MPV were discovered at the prototype stage. First and foremost, the sensor is somewhat less man-portable in practice than on paper. The transmitter and receiver assemblies have sizes and weights that result in a sensor head that is simply too large and heavy. The boom is attached to the head in a way that places the latter too far from the operator, hampering the usability of the sensor as much as the fact that the data acquisition system requires a tether. The ArcSecond positioning system described in Section II-C has satisfactory precision over a short baseline but was found to require rather too much attention; it failed to produce usable data when one of the three ASI transmitters was obscured, which means that the system may lose much of its usefulness in treed landscapes; it also is not, and will likely never be, commercially available. Finally, the top receiver, R0, is always much farther from any buried target than the other four and of necessity detects a much weaker signal; the low SNR may result in data that in some cases can compromise the quality of the rest of the collected information, outweighing the gain in data diversity that motivated its original inclusion.

The MPV-II, a new incarnation of the MPV, has been designed and developed (again by G&G Sciences) with these issues in mind; it appears on Fig. 14. Its receiver cubes are smaller



Fig. 14. A new incarnation of the MPV, the MPV-II, features a smaller and lighter head, a single transmitter coil, and a positioning system that uses the transmitter as a beacon. The sensor incorporates an enhanced RTK GPS receiver and uses an iPad to communicate with the data acquisition system. Its head is about 50 cm in diameter.

(with 8-cm sides as opposed to 10 cm, and with coil height 3 cm) and have been set closer together, with a center-to-center separation of 18.44 cm (down from 39.3 cm). The new system has one transmitter coil instead of two, thus shedding much weight; the 21-turn, 7.74 cm tall coil has diameter 49.68 cm (one-third smaller than the original) and is centered with the receiver assembly. In all, the weight of the new device is about 12 lb, which makes it less than half as heavy as the 23-lb original MPV. The ergonomic enhancements go beyond the reduction in size and weight. The sensor head of the new instrument is only about a foot away from the operator. The setup is also more balanced, for greater ease of operation. The system uses an Apple iPad to allow wireless communication with the data acquisition system (and potentially to enhance the user interface).

For positioning, the MPV-II has a real-time-kinematic (RTK) GPS system [52] with a horizontal uncertainty of  $\pm 2$  cm. The device also incorporates an electronic compass that gives its 3D attitude at all times. For enhanced accuracy, and for situations in which there is no GPS access, a new positioning system is being implemented that uses the primary field of the transmitter as a beacon; the field information is collected by two receivers separated by 149.35 cm and (at this point) tethered to the sensor head. This is similar to the positioning system for the GEM-3D+ frequency-domain sensor [34] and is depicted in Fig. 14.

A final difference between the MPV and the MPV-II is that the zeroth receiver has become the fifth; it is now located behind R1 on the same horizontal plane as the others. This new configuration of receivers should allow the experimental computation of field gradients.

Fig. 15 shows an example dipole inversion from an MPV-II measurement. The data were collected by two of the authors (BEB and NL) at the Yuma Proving Ground, AZ, in October of 2010. A 40-mm projectile was interred 22 cm below the ground, vertical facing down; the MPV-II was placed flat at a set of nine points not on a grid (see Fig. 14). The inverted depth and dip angle are respectively 22.8 cm and  $268^\circ$ . For comparison we show a Sky Hanover measurement (Section III-B2) with two copies of that projectile “buried” 25 cm away from the sensor and separated by 40 cm. The inverted locations are within 2 cm of the ground truth. The polarizabilities are very close in all three

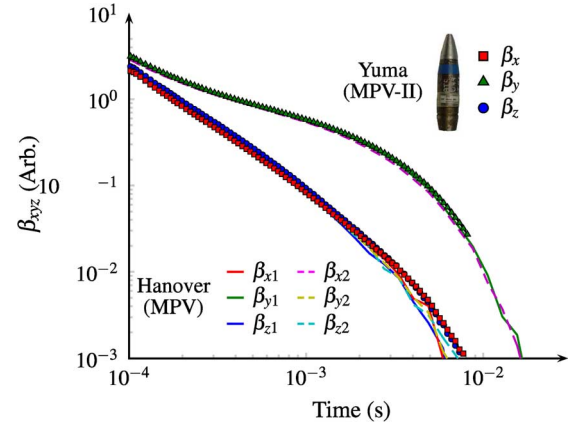


Fig. 15. Magnetic polarizabilities inverted from Yuma Proving Ground MPV-II data (markers). The target is a 40-mm projectile buried 22 cm below ground. The inverted location and orientation agree well with the ground truth. For comparison we include the polarizabilities (solid and dashed lines) extracted from a two-target MPV measurement carried out, using the same munition, at Sky Research in Hanover.

cases, lending credence to both instruments and to the inversion procedure.

## V. CONCLUSION

In this paper we have presented the MPV sensor, a time-domain EMI instrument designed for the detection, identification, and discrimination of buried objects, in particular unexploded ordnance. We have seen that the diverse, high-quality data provided by the MPV can be combined with the tensor dipole model to locate and characterize subsurface targets accurately. The data consistently allow the simultaneous identification of multiple targets.

The newer, streamlined MPV-II is expected to take over the MPV's original role in UXO remediation, as it produces data of similar quality (and improving) and comes closer to being truly portable and usable in forbidding terrains. The current system, however, is expected to keep being relevant in humanitarian and military-environmental contexts. For example, it has been proposed to use the current MPV as part of a robotic system that could be used to detect roadside bombs in theaters of conflict and, in friendlier contexts, for pipe detection. In fact, the instrument has already been used as part of a humanitarian demining operation in Laos.

## APPENDIX

### NUMERICAL IMPLEMENTATION OF THE DIPOLE MODEL

As mentioned in Section II, at every location  $\mathbf{r}_j$  and time gate  $t_k$  the MPV provides 15 data points, corresponding to the flux in the  $\nu$ th direction through the  $\mu$ th receiver  $R_\mu$ . These we call  $H_{\mu\nu}(\mathbf{r}_j, t_k)$ , in analogy with (14). If measurements have been taken at  $N_{\text{pt}}$  different locations using  $N_{\text{tg}}$  time gates, we can stack the collected information in a two-dimensional array  $\mathbf{H}^{\text{sc}}$  of size  $(N_{\text{pt}} \cdot 5 \cdot 3) \times N_{\text{tg}}$  with elements

$$\mathbf{H}^{\text{sc}} = \begin{bmatrix} H_z^{\text{sc}} \\ H_y^{\text{sc}} \\ H_x^{\text{sc}} \end{bmatrix} \quad (17)$$

where

$$\mathbf{H}_\nu^{\text{sc}} = \begin{bmatrix} H_{0\nu}(\mathbf{r}_1, t_1) & \cdots & H_{0\nu}(\mathbf{r}_1, t_{N_{\text{tg}}}) \\ \vdots & \vdots & \vdots \\ H_{0\nu}(\mathbf{r}_{N_{\text{pt}}}, t_1) & \cdots & H_{0\nu}(\mathbf{r}_{N_{\text{pt}}}, t_{N_{\text{tg}}}) \\ H_{1\nu}(\mathbf{r}_1, t_1) & \cdots & H_{1\nu}(\mathbf{r}_1, t_{N_{\text{tg}}}) \\ \vdots & \vdots & \vdots \\ H_{4\nu}(\mathbf{r}_{N_{\text{pt}}}, t_1) & \cdots & H_{4\nu}(\mathbf{r}_{N_{\text{pt}}}, t_{N_{\text{tg}}}) \end{bmatrix}. \quad (18)$$

Knowledge of the location  $\mathbf{r}'$  of the responding dipole and of the MPV geometry displayed in Fig. 2 allows the computation of the  $(N_{\text{pt}} \cdot 5 \cdot 3) \times 3$  arrays

$$\mathbf{R}_v \equiv [\mathbf{X} \quad \mathbf{Y} \quad \mathbf{Z}] \quad \text{and} \quad \mathbf{H}^{\text{pr}} \equiv [\mathbf{H}_x^{\text{pr}} \quad \mathbf{H}_y^{\text{pr}} \quad \mathbf{H}_z^{\text{pr}}] \quad (19)$$

along with  $\mathbf{R}$ , the row-by-row 2-norm of  $\mathbf{R}_v$ , in terms of which we can define the Green matrix

$$\mathbf{G} = \begin{bmatrix} \mathbf{G}_z \\ \mathbf{G}_y \\ \mathbf{G}_x \end{bmatrix} \quad (20)$$

where

$$\mathbf{G}_z = \int_{\mathbf{R}_\mu} ds \frac{1}{4\pi R^5} \otimes [3\mathbf{Z}\mathbf{X} \quad 3\mathbf{Z}\mathbf{Y} \quad 3\mathbf{Z}^2 - \mathbf{R}^2] \otimes \mathbf{H}^{\text{pr}} \quad (21a)$$

$$\mathbf{G}_y = \int_{\mathbf{R}_\mu} ds \frac{1}{4\pi R^5} \otimes [3\mathbf{Y}\mathbf{X} \quad 3\mathbf{Y}^2 - \mathbf{R}^2 \quad 3\mathbf{Y}\mathbf{Z}] \otimes \mathbf{H}^{\text{pr}} \quad (21b)$$

$$\mathbf{G}_x = \int_{\mathbf{R}_\mu} ds \frac{1}{4\pi R^5} \otimes [3\mathbf{X}^2 - \mathbf{R}^2 \quad 3\mathbf{X}\mathbf{Y} \quad 3\mathbf{X}\mathbf{Z}] \otimes \mathbf{H}^{\text{pr}}. \quad (21c)$$

In (21), all array operations (multiplication and raising to positive and negative powers) are carried out element-by-element; the  $\otimes$  operator is shorthand for elementwise multiplication and matrix concatenation corresponding to a row-by-row Kronecker product [53]. The integration over the receiver areas is carried out using two-dimensional Gauss–Legendre quadrature [54] along a third dimension. As defined,  $\mathbf{G}$  has size  $(N_{\text{pt}} \cdot 3 \cdot 5) \times 9$ . We can then solve for the polarizability tensor using the pseudoinverse [55]

$$\mathbf{P} = \arg \min_{\mathbf{M}} \frac{1}{2} \|\mathbf{G}\mathbf{M} - \mathbf{H}^{\text{sc}}\|^2 = \mathbf{G}^+ \mathbf{H}^{\text{sc}}. \quad (22)$$

The resulting  $9 \times N_{\text{tg}}$  array  $\mathbf{P}$  gives the full polarizability matrix at all time gates. (It is also possible to enforce the symmetry of  $\mathbf{B}$  and have  $\mathbf{P}$  have 6 columns instead of 9; the resulting Green matrix is less transparent, however, and we did not find a noticeable improvement in either speed or accuracy.) We then rearrange the elements of  $\mathbf{P}$  into a three-dimensional array of size  $3 \times 3 \times N_{\text{tg}}$  and use a joint-approximate-diagonalization algorithm that finds an orthogonal matrix  $\mathbf{V}$  such that at each time gate  $t_k$

$$\mathbf{P}(t_k) = \mathbf{V}\mathbf{\Lambda}(t_k)\mathbf{V}^T \quad (23)$$

with the desired  $\mathbf{\Lambda}(t_k)$  “as diagonal as possible” [56], [57]. The matrix  $\mathbf{V}$  is an approximation to  $\mathbf{R}_{abc}$ , which gives us the orientation of the target.

As remarked right after (18), the procedure just described assumes that we know the location  $\mathbf{r}'$  of the dipole. The final step in the inversion procedure is to relax that condition and find a now unknown  $\mathbf{r}'$  by optimization. Given a proposed value  $\mathbf{r}'_p$  for the dipole location we can define a “modeled” signal by

$$\mathbf{S}(\mathbf{r}'_p) = \mathbf{G}(\mathbf{r}'_p)\mathbf{P} \quad (24)$$

and minimize the objective function

$$J = \sqrt{\frac{[\text{vec}(\mathbf{S}(\mathbf{r}'_p) - \mathbf{H}^{\text{sc}})]^T \text{vec}(\mathbf{S}(\mathbf{r}'_p) - \mathbf{H}^{\text{sc}})}{[\text{vec}\mathbf{H}^{\text{sc}}]^T \text{vec}\mathbf{H}^{\text{sc}}}} \times 100\%, \quad (25)$$

where the  $\text{vec}$  operator turns a matrix into a column vector by stacking its columns in order [58]. It is not necessary to perform any weighting or regularization. Every function call during the minimization of (25) performs a linear least-squares fit of the form (22), which means that in a sense each proposed dipole location dictates at one stroke the orientation and time-dependent polarizabilities that best enable it to conform to the measured signal.

Any unconstrained optimization routine can in principle be used to extract the optimal  $\mathbf{r}'$ . We have used a subspace trust region algorithm based on an interior-reflective Newton method (implemented in MATLAB as `lsqnonlin`) [59]–[61], a Broyden–Fletcher–Goldfarb–Shanno quasi-Newton method (`fminunc`) [59] and references therein, the Nelder–Mead downhill simplex method (`fminsearch`) [62], and differential evolution (DE), a genetic-style minimization algorithm [63]. We obtain the same results with the different methods. The procedure is also very fast—essentially instantaneous for one-target inversions.

It is straightforward to adapt the method to two-object scenarios by adding columns to the Green matrix and rows to the response array. Equation (22) becomes

$$\begin{bmatrix} \mathbf{P}^1 \\ \mathbf{P}^2 \end{bmatrix} = \arg \min_{\mathbf{M}^1, \mathbf{M}^2} \frac{1}{2} \left\| \begin{bmatrix} \mathbf{G}^1 & \mathbf{G}^2 \end{bmatrix} \begin{bmatrix} \mathbf{M}^1 \\ \mathbf{M}^2 \end{bmatrix} - \mathbf{H}^{\text{sc}} \right\|^2 \\ = [\mathbf{G}^1 \quad \mathbf{G}^2]^+ \mathbf{H}^{\text{sc}} \quad (26)$$

and the minimization yields the two dipole locations  $\mathbf{r}_1, \mathbf{r}_2$ .

#### ACKNOWLEDGMENT

The authors would like to thank D. C. George and J. L. George of G&G Sciences for taking the Vicksburg data of Section III-B1, S. Jensen-Segal and I. Shamatava of Sky Research for taking the Hanover data of Section III-B2, and Dr. L. Pasion, J. Jacobson, and H. Ngo of Sky Research and Dr. L.-P. Song of the University of British Columbia for taking the Vancouver data of Section III-B3.



## REFERENCES

- [1] *Guidance for Surveillance of Injuries Due to Landmines and Unexploded Ordnance*, D. Sethi and E. Krug, Eds., Geneva, Switzerland: World Health Organization, 2000.
- [2] O. O. Bilukha, M. Brennan, and M. Anderson, "Injuries and deaths from landmines and unexploded ordnance in Afghanistan, 2002–2006," *J. Amer. Med. Assoc.*, vol. 298, pp. 516–518, Aug. 2007.
- [3] "Unexploded Ordnance (UXO): An Overview," Federal Advisory Committee for the Development of Innovative Technologies. [Online]. Available: <https://www.denix.osd.mil>, Oct. 1996
- [4] F. S. Grant and G. F. West, *Interpretation Theory in Applied Geophysics*. New York: McGraw-Hill, 1965.
- [5] E. Gasperikova, J. T. Smith, H. F. Morrison, and A. Becker, "Berkeley UXO Discriminator (BUD)," 2007, Paper LBNL-62263.
- [6] E. Gasperikova, J. T. Smith, H. F. Morrison, A. Becker, and K. Kappeler, "UXO detection and identification based on intrinsic target polarizabilities—A case history," *Geophysics*, vol. 74, pp. B1–B8, Jan.–Feb. 2009.
- [7] D. A. Steinhurst, G. R. Harbaugh, J. B. Kingdon, T. Furuya, D. A. Keiswetter, and D. C. George, "EMI array for cued UXO discrimination," ESTCP Project MM-0601 Final Rep., Jul. 2010 [Online]. Available: <http://www.serdp.org/Program-Areas/Munitions-Response/Land/Sensors/MR-200601/MR-200601>
- [8] M. Prouty, "Draft demonstration plan: Detection and classification with the MetalMapper™ at former Camp San Luis Obispo," Geometrics, Inc., San Jose, CA, 2009 [Online]. Available: <http://www.geometrics.com>
- [9] M. Prouty, "MetalMapper System: Camp San Luis Obispo Discrimination Study," ESTCP Project MM-0603 Interim Data Rep., Jul. 2009 [Online]. Available: <http://www.serdp-estcp.org/Program-Areas/Munitions-Response/Land/Sensors/MR-200603/MR-200603>
- [10] D. C. George and J. L. George, "Data Report: Tests of MPV at Vicksburg, February 26 to March 2, 2007," Grand Junction, CO: G&G Sciences Inc., Technical Note 2007-2, 2007 [Online]. Available: <http://www.ggsclences.com>
- [11] F. Shubitidze, J. P. Fernández, B. E. Barrowes, I. Shamatava, and K. O'Neill, "Combining NSMS and high-quality MPV-TD data for UXO discrimination," in *Proc. IEEE Int. Geosci. Remote Sens. Symp.*, Boston, MA, Jul. 2008, pp. 17–20.
- [12] F. Shubitidze, B. E. Barrowes, I. Shamatava, J. P. Fernández, and K. O'Neill, "Data-derived generalized SEA applied to MPV TD data," in *Proc. Appl. Comput. Electromagn. Sympo. (ACES)*, Niagara Falls, ON, Mar.–Apr. 2008.
- [13] F. Shubitidze, B. E. Barrowes, I. Shamatava, J. P. Fernández, and K. O'Neill, "Rapid and accurate estimate of the effect of magnetically susceptible soil on MPV-TD sensor data using the method of images," in *Direct and Inverse Problems of Electromagnetic and Acoustic Wave Theory (DIPED-2008)*, Tbilisi, Georgia, 2008.
- [14] T. M. Grzegorzczuk, B. E. Barrowes, F. Shubitidze, J. P. Fernández, and K. O'Neill, "Simultaneous identification of multiple unexploded ordnance using electromagnetic induction sensors," *IEEE Trans. Geosci. Remote Sens.*, 2011, accepted for publication.
- [15] J. P. Fernández, B. E. Barrowes, K. O'Neill, I. Shamatava, F. Shubitidze, and K. Sun, "A data-derived time-domain SEA for UXO identification using the MPV sensor," in *Proc. SPIE Detection and Sensing of Mines, Explosive Objects, and Obscured Targets XIII*, R. S. Harmon, J. T. Broach, and J. H. Holloway, Jr., Eds., Orlando, FL, Mar. 2008, vol. 6953, pp. 6953–1H.
- [16] F. Shubitidze, B. E. Barrowes, I. Shamatava, J. P. Fernández, and K. O'Neill, "Application of the NSMC model to multi-axis time domain EMI data," in *Proc. SPIE Detection and Sensing of Mines, Explosive Objects, and Obscured Targets XIII*, R. S. Harmon, J. T. Broach, and J. H. Holloway, Jr., Eds., Orlando, FL, Mar. 2008, vol. 6953, p. 6953-2.
- [17] B. E. Barrowes, F. Shubitidze, J. P. Fernández, I. Shamatava, and K. O'Neill, "Man-portable vector EMI instrument data characterization using the NSMS method," in *Proc. SPIE Detection and Sensing of Mines, Explosive Objects, and Obscured Targets XIV*, R. S. Harmon, J. T. Broach, and J. H. Holloway, Jr., Eds., Orlando, FL, Apr. 2009, vol. 7303, pp. 7303–0V.
- [18] F. Shubitidze, D. Karkashadze, J. P. Fernández, B. E. Barrowes, K. O'Neill, T. Grzegorzczuk, and I. Shamatava, "Applying a volume dipole distribution model to next-generation sensor data for multi-object data inversion and discrimination," in *Proc. SPIE Detection and Sensing of Mines, Explosive Objects, and Obscured Targets XV*, R. S. Harmon, J. T. Broach, and J. H. Holloway, Jr., Eds., Orlando, FL, Apr. 2010, vol. 7664, pp. 7664–07.
- [19] B. E. Barrowes, K. O'Neill, T. M. Grzegorzczuk, X. Chen, and J. A. Kong, "Broadband analytical magnetoquasistatic electromagnetic induction solution for a conducting and permeable spheroid," *IEEE Trans. Geosci. Remote Sens.*, vol. 42, no. 11, pp. 2479–2489, Nov. 2004.
- [20] X. Chen, K. O'Neill, T. M. Grzegorzczuk, and J. A. Kong, "Spheroidal mode approach for the characterization of metallic objects using electromagnetic induction," *IEEE Trans. Geosci. Remote Sens.*, vol. 45, no. 3, pp. 697–706, Mar. 2007.
- [21] T. M. Grzegorzczuk, B. Zhang, J. A. Kong, B. E. Barrowes, and K. O'Neill, "Electromagnetic induction from highly permeable and conductive ellipsoids under arbitrary excitation: Application to the detection of unexploded ordnances," *IEEE Trans. Geosci. Remote Sens.*, vol. 46, no. 4, pp. 1164–1176, Apr. 2008.
- [22] L. Carin, H. Yu, Y. Dalichaouch, A. R. Perry, P. V. Czipott, and C. E. Baum, "On the wideband EMI response of a rotationally symmetric permeable and conducting target," *IEEE Trans. Geosci. Remote Sens.*, vol. 39, no. 6, pp. 1206–1213, Jun. 2001.
- [23] T. H. Bell, B. J. Barrow, and J. T. Miller, "Subsurface discrimination using electromagnetic induction sensors," *IEEE Trans. Geosci. Remote Sens.*, vol. 39, no. 6, pp. 1286–1293, Jun. 2001.
- [24] N. Geng, C. E. Baum, and L. Carin, "On the low-frequency natural response of conducting and permeable targets," *IEEE Trans. Geosci. Remote Sens.*, vol. 37, no. 1, pp. 347–359, Jan. 1999.
- [25] J. T. Smith and H. F. Morrison, "Estimating equivalent dipole polarizabilities for the inductive response of isolated conductive bodies," *IEEE Trans. Geosci. Remote Sens.*, vol. 42, no. 6, pp. 1208–1214, Jun. 2004.
- [26] J. T. Smith and H. F. Morrison, "Optimizing receiver configurations for resolution of equivalent dipole polarizabilities *in situ*," *IEEE Trans. Geosci. Remote Sens.*, vol. 43, no. 7, pp. 1490–1498, Jul. 2005.
- [27] L. R. Pasion and D. W. Oldenburg, "A discrimination algorithm for UXO using time-domain electromagnetic induction," *J. Environ. Eng. Geophys.*, vol. 6, pp. 91–102, 2001.
- [28] L. D. Landau, E. M. Lifshitz, and L. P. Pitaevskii, *Electrodynamics of Continuous Media*, 2nd ed. Oxford, U.K.: Pergamon, 1984.
- [29] B. E. Barrowes, K. O'Neill, F. Shubitidze, and J. P. Fernández, "High-fidelity electromagnetic induction instruments and physically complete models," in *Proc. SERDP-ESTCP Partners in Environ. Technol. Tech. Symp. Workshop*, Washington, DC, Dec. 2009.
- [30] W. R. Smythe, *Static and Dynamic Electricity*, 3rd ed. New York: McGraw-Hill, 1968.
- [31] J. A. Stratton, *Electromagnetic Theory*. New York: McGraw-Hill, 1941.
- [32] D. F. Lawden, *Elliptic Functions and Applications*. New York: Springer, 1989.
- [33] R. H. Good, "Elliptic integrals, the forgotten functions," *Eur. J. Phys.*, vol. 22, pp. 119–126, Mar. 2001.
- [34] J. P. Fernández, B. E. Barrowes, K. O'Neill, I. Shamatava, and F. Shubitidze, "A vector handheld frequency-domain sensor for UXO identification," in *Proc. SPIE Detection and Sensing of Mines, Explosive Objects, and Obscured Targets XIV*, R. S. Harmon, J. T. Broach, and J. H. Holloway, Jr., Eds., Orlando, FL, Apr. 2009, vol. 7303, pp. 7303–0W.
- [35] J. D. McNeill and M. Bosnar, "Application of TDEM techniques to metal detection and discrimination: A case history with the new geonics EM-63 fully time-domain metal detector," Geonics Ltd., Mississauga, ON, Tech. Note TN-32, 2000 [Online]. Available: <http://www.geonics.com>
- [36] D. D. Snyder, "Technical Report: Precision position and attitude measurements: An evaluation of the integration of the ArcSecond 'Indoor GPS' system into the MPV," Snyder Geoscience, Inc., Grand Junction, CO, 2007.
- [37] I. Y. Bar-Itzhack and K. A. Fegley, "Orthogonalization techniques of a direction cosine matrix," *IEEE Trans. Aerosp. Electron. Syst.*, vol. AES-5, no. 5, pp. 798–804, Sep. 1969.
- [38] J.-L. Boiffier, *The Dynamics of Flight: The Equations*. Chichester, U.K.: Wiley, 1998.
- [39] K. Sun, K. O'Neill, B. E. Barrowes, J. P. Fernández, F. Shubitidze, I. Shamatava, and K. Paulsen, "Dumbbell dipole model and its application in UXO discrimination," in *Proc. SPIE Detection and Remediation Technologies for Mines and Minelike Targets XI*, J. T. Broach, R. S. Harmon, and J. H. Holloway, Jr., Eds., Orlando, FL, Apr. 2006, vol. 6217, p. 621706.
- [40] *Electromagnetic Methods in Applied Geophysics: Volume 1, Theory*, ser. Investigations in Geophysics, M. N. Nabighian, Ed. Tulsa, OK: Society of Exploration Geophysicists, 1997.
- [41] A. A. Kaufman, *Geophysical Field Theory and Method, Part C: Electromagnetic Fields II*. San Diego, CA: Academic, 1994.
- [42] L.-P. Song, F. Shubitidze, L. R. Pasion, D. W. Oldenburg, and S. D. Billings, "Computing transient electromagnetic responses of a metallic object using a spheroidal excitation approach," *IEEE Geosci. Remote Sens. Lett.*, vol. 5, no. 7, pp. 359–363, Jul. 2008.

- [43] R. N. Bracewell, *The Fourier Transform and Its Applications*, 2nd ed. New York: McGraw-Hill, 1978.
- [44] L. R. Pasion, S. D. Billings, D. W. Oldenburg, and S. E. Walker, "Application of a library based method to time domain electromagnetic data for the identification of unexploded ordnance," *J. Appl. Geophys.*, vol. 61, pp. 279–291, Mar. 2007.
- [45] J. R. Wait and K. P. Spies, "Quasi-static transient response of a conducting permeable sphere," *Geophysics*, vol. 34, pp. 789–792, Oct. 1969.
- [46] P. B. Weichman, "Universal early-time response in high-contrast electromagnetic scattering," *Phys. Rev. Lett.*, vol. 91, p. 143908, Oct. 2003.
- [47] P. B. Weichman, "Surface modes and multipower-law structure in the early-time electromagnetic response of magnetic targets," *Phys. Rev. Lett.*, vol. 93, p. 023902, Jul. 2004.
- [48] F. Shubitidze, J. P. Fernández, I. Shamatava, L. R. Pasion, B. E. Barrowes, and K. O'Neill, "Application of the normalized surface magnetic source model to a blind unexploded ordnance discrimination test," *ACES J.*, vol. 25, pp. 89–98, Jan. 2010.
- [49] Y. Das, J. E. McFee, J. Toews, and G. C. Stuart, "Analysis of an electromagnetic induction detector for real-time location of buried objects," *IEEE Trans. Geosci. Remote Sens.*, vol. 28, no. 5, pp. 278–288, May 1990.
- [50] Tibtech Innovations, "Properties table of stainless steel, metals and other conductive materials," 2010 [Online]. Available: <http://www.tibtech.com/conductivity.php>
- [51] J. P. Fernández, B. E. Barrowes, K. O'Neill, I. Shamatava, and F. Shubitidze, "Realistic subsurface anomaly discrimination using electromagnetic induction and an SVM classifier," *EURASIP J. Adv. Signal Process.*, vol. 2010, p. 305890, 2010.
- [52] T. Takasu and A. Yasuda, "Development of the low-cost RTK-GPS receiver with an open source program package RTKLIB," in *Int. Symp. GPS/GNSS*, Jeju, Korea, Nov. 2009.
- [53] R. A. Horn and C. R. Johnson, *Topics in Matrix Analysis*. Cambridge, U.K.: Cambridge Univ. Press, 1994.
- [54] L. N. Trefethen, *Spectral Methods in Matlab*. Philadelphia, PA: SIAM, 2000.
- [55] R. C. Aster, B. Borchers, and C. H. Thurber, *Parameter Estimation and Inverse Problems*. Burlington, MA: Elsevier, 2005.
- [56] J.-F. Cardoso and A. Souloumiac, "Jacobi angles for simultaneous diagonalization," *SIAM J. Matrix Anal. Appl.*, vol. 17, pp. 161–164, Jan. 1996.
- [57] J.-F. Cardoso, "Perturbation of joint diagonalizers. Ref# 94d027," Télécom Paris, Tech. Rep., 1994.
- [58] K. B. Petersen and M. S. Pedersen, "The Matrix Cookbook," 2007 [Online]. Available: <http://matrixcookbook.com>
- [59] *Optimization Toolbox for Use With Matlab*. Natick, MA: MathWorks, 2000.
- [60] T. F. Coleman and Y. Li, "On the convergence of interior-reflective Newton methods for nonlinear minimization subject to bounds," *Math. Program.*, vol. 67, pp. 189–224, Oct. 1994.
- [61] T. F. Coleman and Y. Li, "An interior trust region approach for nonlinear minimization subject to bounds," *SIAM J. Optim.*, vol. 6, pp. 418–445, May 1996.
- [62] W. H. Press, S. A. Teukolsky, W. A. Vetterling, and B. P. Flannery, *Numerical Recipes in C*, 2nd ed. Cambridge, U.K.: Cambridge Univ. Press, 1992.
- [63] R. Storn and K. Price, "Differential evolution—A simple and efficient heuristic for global optimization over continuous spaces," *J. Global Optim.*, vol. 11, pp. 341–359, Dec. 1997.



**Juan Pablo Fernández** received the degree of Física from the Universidad de los Andes, Bogotá, Colombia, in 1990, the Ph.D. degree in theoretical low-temperature physics from the University of Massachusetts, Amherst, in 2004, and the M.S. degree in engineering sciences from the Thayer School of Engineering, Dartmouth College, Hanover, NH, in 2007.

He has taught physics, mathematics, astronomy, Spanish, and scientific writing at several universities in Colombia and the United States and has worked as a writer, editor, and translator. He has been a Research Associate with the Thayer School of Engineering and is, currently, a Research Consultant with the Cold Regions Research and Engineering Laboratory, Hanover, NH. In June

2010, he was a Visiting Research Scientist at the Center for Adaptive Behavior and Cognition, Max Planck Institute for Human Development, Berlin, Germany. He has performed research on the theory of Bose–Einstein condensation and currently dedicates his efforts to the discrimination of unexploded ordnance using electromagnetic induction and machine learning.

Dr. Fernández is a member of the Applied Computational Electromagnetics Society. He was the recipient of a "Francisco de Paula Santander" grant for creative writing from the Instituto Colombiano de Cultura in 1990, was short-listed for the Premio Nacional de Literatura in 1998, and received the Eugene M. Isenberg Award from the Isenberg School of Management at the University of Massachusetts in 1997 and 1998.



**Benjamin E. Barrowes** (M'99) received the B.S. and M.S. degrees in electrical engineering from Brigham Young University, Provo, UT, in 1999 and the Ph.D. degree from the Massachusetts Institute of Technology (MIT), Cambridge, in 2004.

During 2004–2005, he was a Director's funded Postdoc at Los Alamos National Laboratory in the Physics Division. He is currently a Physicist with the Cold Regions Research and Engineering Laboratory, Engineer Research and Development Center, Hanover, NH. His research interests center

on electromagnetic wave theory and modeling with applications including wind-wave interaction, electromagnetic scattering from the sea surface as well as from random media, nanoscale energy generation techniques, computer interface methodologies, electromagnetic induction models for nonspherical geometries, and biological electromagnetic phenomena. Other interests include automatic code conversion/translation and arbitrary precision computing.

Dr. Barrowes was named the top high school math student in the state of Utah (1991), received two Rocky Mountain Space Grant Consortium grants, and was awarded a National Science Foundation graduate fellowship.



**Tomasz M. Grzegorzczak** (SM'07) received the Ph.D. degree from the Laboratoire d'Electromagnetisme et d'Acoustique, École Polytechnique Fédérale de Lausanne (Swiss Federal Institute of Technology), Lausanne, Switzerland, in 2000.

From January 2001 to July 2007, he was a Research Scientist with the Research Laboratory of Electronics, Massachusetts Institute of Technology (MIT), Cambridge, and a Research Affiliate with MIT until January 2011. In 2007, he founded Delpsi, LLC, Newton, MA, where he continues performing

unclassified research for the Department of Defense, as well as various companies and universities. He is an Adjunct Professor at Zhejiang University, Hangzhou, China. He has recently authored a book on metamaterials. His research interests include the use of electromagnetic induction for the detection and classification of unexploded ordnance, biomedical microwave imaging, optical binding and trapping, wave propagation in bianisotropic media, and left-handed metamaterials.

Dr. Grzegorzczak is a member of the Optical Society of America. He has served as an Editor and board member of two international peer-reviewed journals (*The Progress In Electromagnetic Research* and the *Journal of Electromagnetic Waves and Applications*) and one international conference (*The Progress in Electromagnetics Research Symposium*).



**Nicolas Lhomme** received the Ph.D. degree in geophysics, glaciology, and climatology from the University of British Columbia (UBC), Vancouver, Canada, and Université Joseph Fourier, Grenoble, France, in 2004.

He started working on problems related to buried unexploded ordnance (UXO) in 2005 with the UBC Geophysical Inversion Facility. Currently, he is a Geophysicist at Sky Research, Inc., Vancouver. His research interests include the development and testing of methods for the detection and discrimination of UXO using electromagnetic and magnetic data, novel positioning systems, nonlinear inverse theory, and classification.



**Kevin O'Neill** received the B.A. degree (*magna cum laude*) from Cornell University, Ithaca, NY, and the M.A., M.S.E., and Ph.D. degrees from Princeton University, Princeton, NJ.

After a National Science Foundation Postdoctoral Fellowship at the Thayer School of Engineering, Dartmouth College, Hanover, NH, and the U.S. Army Cold Regions Research and Engineering Laboratory (CRREL), he was with CRREL as a Research Civil Engineer. His research has focused on numerical modeling of porous media transport phenomena and of geotechnically relevant electromagnetic problems. He has been a Visiting Fellow at the Department of Agronomy, Cornell University, continues as a Visiting Scientist at the Center for Electromagnetic Theory and Applications at the Massachusetts Institute of Technology, Cambridge, and since 1984, has been on the adjunct faculty of the Thayer School of Engineering. His current work centers on electromagnetic remote sensing of surfaces, layers, and particularly buried objects such as unexploded ordnance.



**Fridon Shubitidze** (A'98–M'04) received the degree of Diploma radio physicist (M.S.) from the Sukhumi branch of Tbilisi State University (TSU), Sukhumi, Republic of Georgia, in 1994 and the Cand.Sci. (Ph.D.) degree in radio physics (applied electromagnetics) from TSU in 1997.

In 1994, he was a Member of the Research Staff of the Laboratory of Applied Electrodynamics, Department of Physics, TSU. At the same time, he was with the Department of Physics and Mathematics, Sukhumi branch of TSU, as a Senior Teacher and became an Associate Professor in 1998. From 1998 to 1999, he was a Postdoctoral Fellow with the National Technical University of Athens, Athens, Greece, performing research in connection with computer simulation of electrostatic discharge, electrodynamic aspects of electromagnetic compatibility, numerical modeling of conformal antennas, electromagnetic wave scattering, field visualization and identification of objects by scattered field analysis, investigation of wave propagation through anisotropy, plasma, and chiral media, and innovative numerical methods. From June to August 2005, he was a Visiting Scientist at the Department of Earth and Ocean Science, University of British Columbia, Vancouver, BC, Canada. He is currently a Research Professor with the Thayer School of Engineering, Dartmouth College, Hanover, NH. His current work interests focus on numerical modeling of forward and inverse electromagnetic scattering by subsurface metallic objects, investigation of global magnetoquasistatic fields due to ionospheric currents, and electrostatic fields' effects on robotic and construction systems for Mars and Lunar exploration.